

Exotic Electronic Properties of 2D Nanosheets Isolated from Liquid Phase Exfoliated Phyllosilicate Minerals

Cencen Wei, Abhijit Roy, Manoj Tripathi, Adel K.A. Aljarid, Jonathan P. Salvage, S. Mark Roe, Raul Arenal, and Conor S. Boland*

Spectrally inactive, electrically insulating, and chemically inert are adjectives broadly used to describe phyllosilicate minerals like mica and chlorite. Here, the above is disproved by demonstrating aqueous suspensions of liquid exfoliated nanosheets from five bulk mica types and chlorite schist. Nanosheet quality is confirmed via transmission electron and X-ray photoelectron spectroscopies, as well as electron diffraction. Through Raman spectroscopy, a previously unreported size- and layer-dependent spectral fingerprint is observed. When analyzing the high-yield suspensions ($\approx 1 \text{ mg mL}^{-1}$) through UV-vis spectroscopy, all phyllosilicates present bandgap (E_g) narrowing from $\approx 7 \text{ eV}$ in the bulk to $\approx 4 \text{ eV}$ for monolayers. Unusually, the bandgap is inversely proportional to the areal size (A) of the nanosheets, measured via atomic force microscopy. Due to an unrecorded quantum confinement effect, nanosheet electronic properties scale toward semiconducting behavior (bandgap $\approx 3 \text{ eV}$) as nanosheet area increases. Furthermore, modeling X-ray diffraction spectra shows that the root cause of the initial bandgap narrowing is lattice relaxation. Finally, with their broad range of isomorphically substituted ions, phyllosilicate nanosheets show remarkable catalytic properties for hydrogen production.

to MXenes,^[7] their unique structural composition, surface chemistry, and broad range of electronic properties have been vital to the acceleration of new-age electronic technologies. Of particular interest are 2D materials in the liquid phase that present morphology-dependent electronic properties, giving rise to processable inks with finely tuned parameters.^[8]

Phyllosilicates are a family of naturally occurring layered materials that consist of stacked 2D silicate sheets held together by van der Waals forces. One well-known member of this family, mica, is widely reported to be electrically insulating and highly inert.^[9] Historically, mica is one of the oldest dielectric materials known and possesses a large bandgap (E_g) of $\approx 7.85 \text{ eV}$ with a dielectric constant between 6 and 9.^[10] However, proof-of-concept work via mechanical exfoliation (ME)^[11] and theoretical calculations^[11f,12] have shown that mica presents an E_g that is highly dependent on layer number due to an unquantified lattice relaxation effect.^[12b] Through the


deposition of ME nanosheets onto electrically conductive substrates, current-voltage curves generated via Conductive Atomic Force Microscopy (C-AFM) were applied to infer information about E_g 's layer dependence. Previously, Kim et al. showed that muscovite mica's E_g decreased from $\approx 7 \text{ eV}$ in the bulk to $\approx 2.5 \text{ eV}$ for a bilayer nanosheet.^[11f] With values as low as $\approx 1.6 \text{ eV}$ reported for a monolayer of phlogopite mica in Islam et al.'s ME work.^[11e]

1. Introduction

Over the past two decades, 2D materials,^[1] due to their unparalleled properties and high potential for application, have had a profound influence on a wide range of research fields as far reaching as bioengineering^[2] to electrochemistry.^[3] From graphene^[4] to transition metal dichalcogenides (TMDs),^[5] layered hydroxides^[6]

C. Wei, M. Tripathi, A. K. Aljarid, C. S. Boland
School of Mathematical and Physical Sciences
University of Sussex
Brighton BN1 9QH, UK
E-mail: c.s.boland@sussex.ac.uk

A. Roy, R. Arenal
Instituto de Nanociencia y Materiales de Aragon (INMA)
CSIC-Universidad de Zaragoza
Zaragoza 50009, Spain

 The ORCID identification number(s) for the author(s) of this article can be found under <https://doi.org/10.1002/adma.202303570>

© 2023 The Authors. Advanced Materials published by Wiley-VCH GmbH. This is an open access article under the terms of the Creative Commons Attribution License, which permits use, distribution and reproduction in any medium, provided the original work is properly cited.

DOI: 10.1002/adma.202303570

A. Roy, R. Arenal
Laboratorio de Microscopias Avanzadas (LMA)
Universidad de Zaragoza
Calle Mariano Esquillor, Zaragoza 50018, Spain

J. P. Salvage
School of Pharmacy and Biomolecular Sciences
University of Brighton
Brighton BN1 9PH, UK

S. M. Roe
School of Life Sciences
University of Sussex
Brighton BN1 9QH, UK
R. Arenal
ARAID Foundation
Zaragoza 50018, Spain

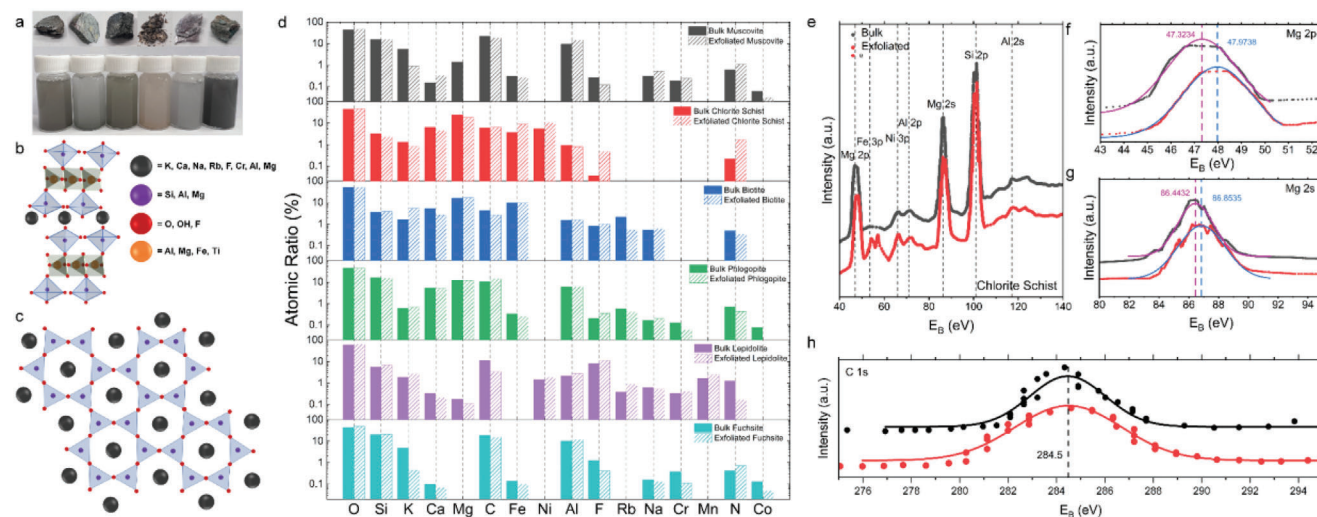


Figure 1. Chemical composition of phyllosilicate nanosheets. a) bulk micas (top) and aqueous suspensions (bottom) of muscovite, chlorite schist, biotite, phlogopite, lepidolite, and fuchsite (left to right). b, c) Partial side on and top down view of basic micene and chlone bilayer (b) and monolayer (c) structure, respectively, with annotated ionic substitutions listed. d) Chemical composition of bulk and exfoliated phyllosilicates reported as atomic ratio from XPS. e) XPS spectra of chlorite schist presented blue shifting due to the exfoliation step. f, g) Explicit look at shifting in 2p (f) and 2s (g) atomic level spectral peaks associated with interlayer Mg^{2+} cations. Solid lines are peak fitting curves. h) XPS spectra of C 1s reference peak for bulk and exfoliated chlorite schist. Dashed line is the expected value of the peak, $E_B \approx 284.5$ eV.

However, these experimental values greatly differ from those predicted by density functional theory (DFT). Through DFT, the E_g of a monolayer of mica was predicted to be between ≈ 3.5 and ≈ 4.5 eV.^[11f,12] To date, these discrepancies have continued to go unexplained.

One issue hindering our understanding of these electronic properties can be attributed to the limitations associated with currently applied methods for the scalable production of phyllosilicate nanosheets. Many techniques utilize surface functionalization, causing electron scattering, which would mask any observation of band narrowing.^[13] Furthermore, phyllosilicate nanosheets are difficult to characterize as they appear to be spectrally inactive and are “invisible” when applying common techniques like Raman spectroscopy.^[14] Additionally, as phyllosilicates have similar structures, it is incorrectly assumed that all material types have the same properties. As such, many studies that apply phyllosilicate materials do not generally differentiate between what type was applied, using generic terms like mica.^[11b,c,13e–g,15] This is akin to labeling all TMDs as just a TMD.

Here, we show that by applying liquid phase exfoliation (LPE), a more thorough investigation of phyllosilicate nanosheet properties was enabled. Through LPE, defect free suspensions of mica and chlorite schist were applied to study these largely overlooked materials. We found that due to the abundant range of ion substitutions in phyllosilicates, specific material types inherently presented individualized properties. Applying a broad range of microscopy techniques, we confirmed the production of few layered nanosheets and explored the effect of centrifugation procedures on nanosheet dimensions. Through spectroscopy techniques, we extrapolated information with regard to the bandgap and its dependence on nanosheet dimension. Through modeling these results, we produced a full description of the mechanisms that controlled bandgap variations. We thus demonstrated that our method of investigation yielded fundamental informa-

tion with regards to both the structural and electronic properties of this untapped family of 2D materials. Finally, we showed that phyllosilicate nanosheet networks are in fact highly reactive and can be applied as effective electrochemical catalysis for the hydrogen evolution reaction (HER). We report that the performances of phyllosilicate nanosheets superseded many commonly applied 2D materials.

2. Results and Discussion

2.1. Liquid Exfoliation of Bulk Phyllosilicates

The phyllosilicate family encompasses four main subgroups of naturally occurring layered materials: serpentines, clays, chlorite, and micas. With the mica subgroup being made up of five material types: muscovite, biotite, phlogopite, lepidolite, and fuchsite.^[16] Here, we take raw mica and chlorite minerals (six total materials) and perform a series of cleaning steps to isolate powders. Taking these cleaned powders, we then performed LPE on them to create nanosheet suspensions (Figure 1a). The basic structure of all isolated mica and chlorite nanosheets is summarized in Figure 1b, c, where individual sheets are comprised of three stacked atomic planes.^[11a] The central plane is an octahedral (O) layer consisting of O^{2-} , F^- , Cl^- , or OH^- anions at the vertices of the octahedral. This plane can act as an interstitial solid solution and can have a plethora of ions (i.e., Mg^{2+} , Fe^{2+} , Al^{3+} , Ti^{2+} , and Si^{4+}) coordinated at the center of the octahedral.^[16,17] The two outermost planes are interconnected six-member rings of SiO_4^{4-} tetrahedrons (T). These planes can also act as interstitial solid solutions, which allow for isomorphic substitutions of the Si^{4+} cations coordinated at each tetrahedron's center. These substitutions include cations such as Mg^{2+} , Fe^{2+} , and Al^{3+} .^[16,17] With these substitutions, a net negative charge in the tetrahedral layer can occur due to an imbalance in the

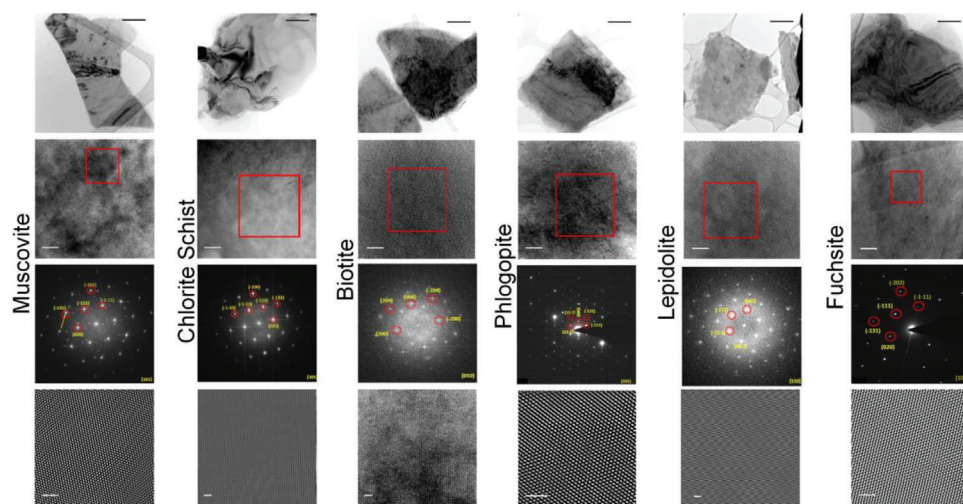


Figure 2. Microscopic analysis of phyllosilicate nanosheets. Low-resolution TEM images of few layered phyllosilicate nanosheets (top row) with a zoomed in view of the basal plane structure (second row). Electron diffraction and fast-Fourier transform (FFT) patterns (third row), with peaks labelled according to their respective Miller indices, and high-resolution TEM and inverse FFT (IFFT) images of lattice structure (bottom row) were taken from a selected area (red square) on each nanosheet. For each column, the scale bars are 200, 10, and 1 nm from the top to bottom, respectively.

oxidation states between the substituted ions and the ions they replace.^[11a,18] This charge is generally compensated by intercalated cations (*M*), such as Ca^{2+} , K^+ , Na^+ , Rb^+ , Cr^{3+} , Al^{3+} , and Mg^{2+} , between the tri-plane sheets in their stacked heterostructures. We confirmed that the elemental composition of both the cleaned bulk materials and the isolated nanosheets was consistent with past works in Figure 1d through X-ray photoelectron spectroscopy (XPS).^[19] Furthermore, we note that the atomic% of elements remains consistent between bulk and exfoliated materials. Thus, confirming that no modifications as a result of the exfoliation step occurred. Examining the XPS spectra of our phyllosilicate materials (Figure 1e; Figures S1–S12, Supporting Information), we note that binding energies (E_B) associated with the intercalated ions shifted toward higher values with exfoliation. Specifically looking at chlorite schist in Figure 1f,g, we note that E_B associated with Mg 2p and Mg 2s peaks shifted by ≈ 0.6 and ≈ 0.4 eV, respectively, when compared to the bulk values. A similar magnitude of intercalated ion E_B shifting was reported in ME muscovite, where a ≈ 0.3 and ≈ 0.4 eV shifting in the K 2p_{3/2} and K 2p_{1/2} peaks was observed, respectively. Though no shifting in the Ni, Al, or Fe peaks associated with intra-sheet substitutions was observed in Figure 1e, we confirm that no artificial spectra shifting occurred by investigating the C 1s reference peak. In Figure 1h, the E_B of C 1s for both bulk and exfoliated chlorite schist resided at the expected value of ≈ 284.5 eV. Thus confirming delamination's effect on the E_B of intercalated ions. Previously, upward shifting in an exfoliated phyllosilicate's intercalated ion peaks was indicative of band tail states forming, which inferred a decrease in bandgap.^[11f]

2.2. Quantifying Exfoliation

Taking our phyllosilicate suspensions, we confirm through low-resolution conventional transmission electron microscopy (TEM) the production of nanosheets via LPE. In the top row of

Figure 2, we present representative images of a few layer micene and chlorene nanosheets that confirm both the layered structure of the materials and their high quality. In the second row of Figure 2, high-resolution TEM images show the uniform structure of the basal plane of our nanosheets, with the red boxes denoting regions in which electron diffraction and fast Fourier transform (FFT) patterns were extrapolated (third row), allowing us to label the peaks with their Miller (*hkl*) indices. Lattice-resolved high resolution TEM and inverse FFT (iFFT) images in the bottom row of Figure 2 show that the basal planes of our nanosheets have a well-ordered structure with no signs of physical defects or lattice distortion.

To examine the exfoliation mechanism, we applied cascade centrifugation to produce suspensions containing quantized size fractions of nanosheets.^[20] By drop-casting our size-selected suspensions onto a silicon substrate, Atomic Force Microscopy (AFM) was applied to confirm the presence of a few layered nanosheets (Figure 3a). As a function of relative centrifugal force (RCF) in Figure 3b, we were able to isolate nanosheets with decreasing mean dimensions (Figure S13, Supporting Information). Through examining the line profiles of individual nanosheets measured via AFM, information on mean lateral length ($\langle L \rangle$, the largest edge to edge distance), width ($\langle W \rangle$, the dimension perpendicular to length), and thickness ($\langle t \rangle$, the line profile height) was extrapolated (Figures S14–S25, Supporting Information). In general, nanosheet $\langle L \rangle$ and $\langle W \rangle$ decreased from ≈ 50 to ≈ 10 nm as RCF increased from 0.12 to 0.48 g. For a similar RCF range, nanosheet $\langle t \rangle$ decreased from ≈ 4 to ≈ 1.6 nm. In terms of layer number, taking a previously reported value of monolayer thickness being ≈ 1 nm,^[13f] $\langle t \rangle$ values corresponded to nanosheets being ≈ 4 to ≈ 1 layers when taking surfactant coverage into consideration. Furthermore, in Figure 3c, nanosheet area ($\langle A \rangle$, described as $\langle L \times W \rangle$) decreased with RCF from ≈ 1000 to ≈ 200 nm² for all nanosheet types. Like other liquid exfoliated nanosheet systems, in Figure 3d,e, both $\langle L \rangle$ and $\langle W \rangle$ scaled proportionally with $\langle t \rangle$.^[21] When assuming that layer

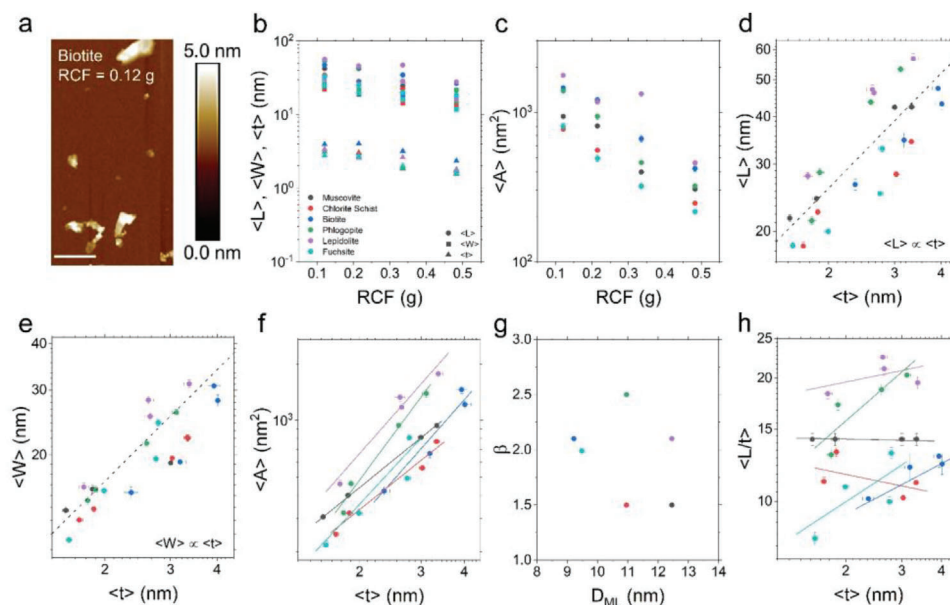


Figure 3. AFM statistical investigation of liquid exfoliated phyllosilicates. a) Representative AFM image of size selected biotite nanosheets. Scale bar 100 nm. b) Mean length ($\langle L \rangle$), width ($\langle W \rangle$) and thickness ($\langle t \rangle$) of nanosheets decreasing as a function of relative centrifugal force (RCF). c) Mean nanosheet area ($\langle A \rangle$), that is, $\langle L \times W \rangle$ as a function of centrifugal force similarly decreased with increasing RCF. d, e) Mean length (d) and width (e) versus mean thickness were directly proportional to one another (i.e., scaled according to a power law with exponent of 1 in both cases, dashed lines). f) Mean nanosheet area as a function of mean thickness presented individualistic power-law scaling that provided insight into the exfoliation mechanism associated with each nanosheet type. g) Scaling exponent β from (f) as a function of the characteristic lateral size associated with each monolayer type (D_{ML}) calculated from Equation 1. h) Aspect ratio (i.e., L/t) as a function of nanosheet thickness. Solid lines are fit to visually display slope of each dataset.

number is roughly equal to t , a simple power-law scaling can be applied that relates $\langle A \rangle$ to the projected monolayer length for a nanosheet (D_{ML}) by^[21]

$$A = D_{ML}^2 \langle t \rangle^\beta \quad (1)$$

where β is a scaling exponent whose value is dictated by the material being exfoliated and the mechanism of exfoliation. In Figure 3f, fits for Equation 1 were found to closely overlay $\langle A \rangle$ versus $\langle t \rangle$ data, with extrapolated values for the scaling exponent β plotted as a function of calculated D_{ML} values in Figure 3g. For our phyllosilicate nanosheets, β was found to vary between ≈ 1.5 and ≈ 2.5 , with values for D_{ML} between ≈ 9 and ≈ 13 nm. Both values here were consistent with graphene, TMDs, and layered hydroxides, which reported values of β between ≈ 1.5 and ≈ 3 , while D_{ML} varied between ≈ 1 and ≈ 20 nm.^[21] Specifically, we find that the predicted D_{ML} values for our phyllosilicate nanosheets matched L values measured for monolayers via AFM. For aspect ratio ($\langle L \rangle / \langle t \rangle$) plotted against $\langle t \rangle$ in Figure 3h, $\langle L \rangle / \langle t \rangle$ was generally > 10 for all nanosheet thicknesses, confirming our materials' sheet-like shape. In comparison to LPE nanosheets of graphene, TMDs, and layered hydroxides of a similar layer number range between 1 and 5, we find our values of $\langle L \rangle / \langle t \rangle$ to be quite high. For these common layered materials, $\langle L \rangle / \langle t \rangle$ was generally between ≈ 2 and ≈ 3.5 .^[21] We note that for phyllosilicates with $\beta > 2$, as standard for LPE, $\langle L \rangle / \langle t \rangle$ decreased with $\langle t \rangle$. However, when $\beta < 2$, $\langle L \rangle / \langle t \rangle$ instead increased with $\langle t \rangle$. This is reported to be a reflection of $\langle L \rangle^\beta \propto \langle t \rangle^\beta$, meaning that $\langle L \rangle / \langle t \rangle \propto \langle t \rangle^{\beta/2-1}$.^[21] This expression eludes to the observed

scaling of $\langle L \rangle / \langle t \rangle$ with $\langle t \rangle$ when $\beta < 2$. This unusual behavior has been previously reported in non-layered^[22] and electrochemically exfoliated^[23] materials. The findings above, nonetheless, prove that phyllosilicate nanosheets do have unique properties, as the mechanisms of exfoliation differ between material types.

2.3. Finding a Spectral Fingerprint

Previously, it was stated that Raman spectroscopy should be excluded from mica investigations due to the weak signal associated with nanosheets.^[14] However, we believe that this was too general of a statement, applying only to single nanosheets. By drop-casting size-selected suspensions of phyllosilicates onto a silicon substrate, thick ($\approx 50 \mu\text{m}$) Raman active networks were formed. By examining networks as opposed to single nanosheets, we obtained Raman spectra that shifted as a function of exfoliation level for muscovite mica in Figure 4A and all other phyllosilicate types in Figures S26–S30 (Supporting Information). Specifically for phyllosilicates, there are a large number of Raman modes associated with the materials due to the diverse range of ions and elements present. For the examined Raman shift range here, generally there can be 17+ vibrational modes present. All of which contribute to the appearance of perceived background noise. However, we still report for every Raman spectrum that all characteristic peaks associated with phyllosilicates were present at Raman shifts of ≈ 470 , ≈ 690 , and $> 800 \text{ cm}^{-1}$.^[24] Wang et al.^[24b] postulate that low temperature measurements

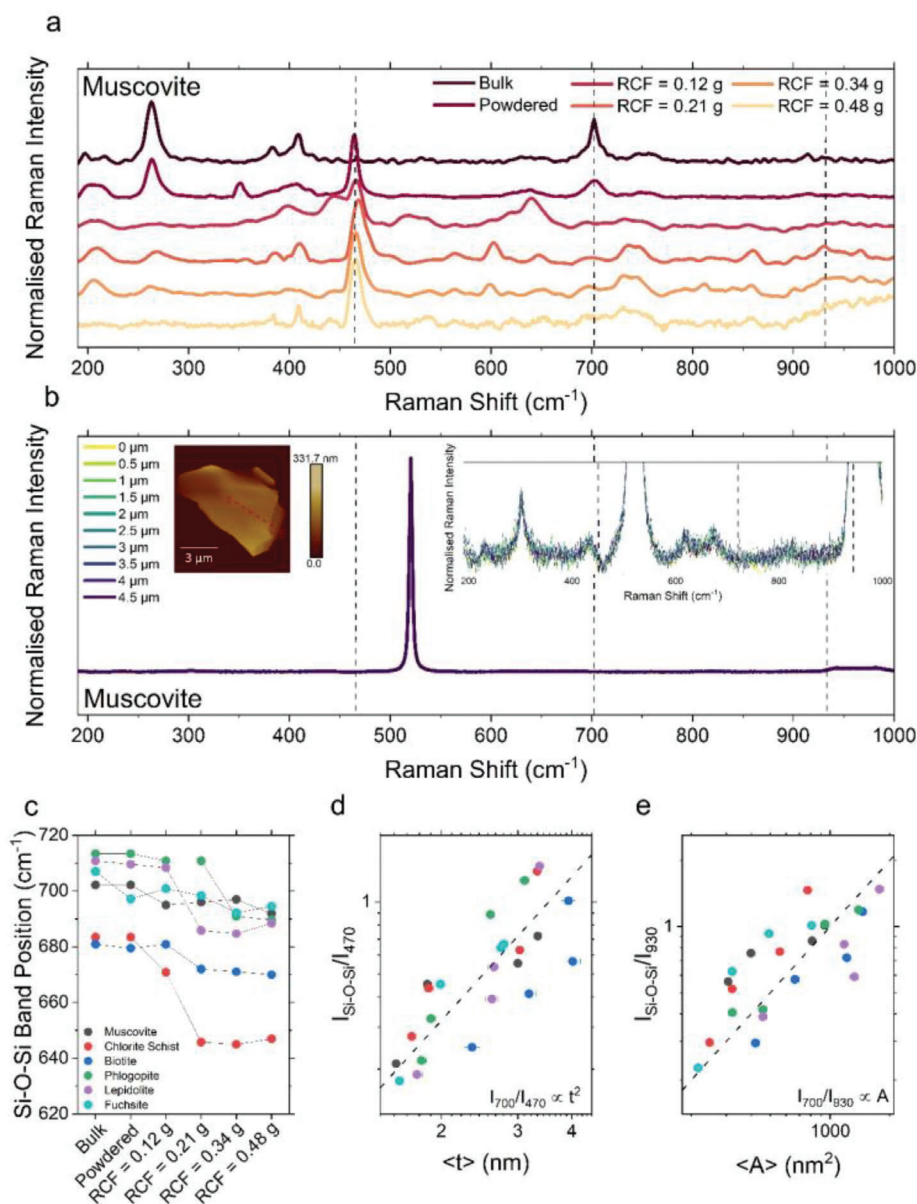


Figure 4. Raman spectral fingerprint of phyllosilicate nanosheet networks. a) Raman spectra based on bulk, powdered and liquid exfoliated nanosheet networks of muscovite show distinct basal plane (dashed lines at ≈470 and ≈700 cm⁻¹) and edge (dashed line at ≈930 cm⁻¹) dependent changes. b) Raman spectral line scan of mechanically exfoliated (ME) quasi-nanosheet of muscovite presents no spectral evidence of mica, with only the characteristic silicon substrate peak at ≈520 cm⁻¹ noted. Left-hand side inset: AFM image of ME muscovite with red-dashed line representing beam path along sheet. Point B denoting the basal plane dominate starting point and the end point E, the edge. Right-hand side inset: zoomed-in view of the Raman spectra as a function of scan distance showed no variation and again was dominated by peaks associated with the silicon substrate. Black-dashed lines represent where the basal plane and edge effect regions noted in mica nanosheet networks should have been observed. c) Raman shift change of characteristic Si-O-Si mode as a function of exfoliation step for each phyllosilicate type. d) Intensity ratio of Si-O-Si mode with basal plane specific changes at ≈470 cm⁻¹ versus mean nanosheet thickness (<t>) followed a power-law scaling with an exponent of 2. e) Intensity ratio of Si-O-Si mode and with nonbridging O band associated with edge effects at ≈930 cm⁻¹ against mean nanosheet area (<A>) scaled according to a power-law scaling with an exponent of 1.

could improve the clarity of the signals associated with these critical modes. However, past work on graphene nanosheet networks has shown that temperature modulation will lead to position and width variations in modes.^[25] In Figure 4b, when measuring a large (>10 μm) bulk-like ME flake, we reconfirmed that the individual material appears Raman inactive. Looking at the Raman spectra as a function of beam location, when

moving the beam from the center of the flake to the edge, the spectra remained unchanged and was dominated by the silicon substrate.

For the nanosheet networks, however, when going from bulk to exfoliated materials at the highest RCF rate of 0.48 g, we report large shifts in the modes. The dominant Si-O-Si mode between ≈660 and ≈720 cm⁻¹,^[24] which is associated with the

basal plane of silicates, was found to redshifted by $\approx 10 \text{ cm}^{-1}$ for all materials (Figure 4c). The location of the Si-O-Si mode was tracked by using the adjacent modes either side of this dominant peak, which are reported to be invariant with chemical and physical composition.^[24b] With respect to intensity, the Si-O-Si mode also saturated as the stage of exfoliation increased. Consequently, the intensity of the modes at 470 cm^{-1} and at shifts $>800 \text{ cm}^{-1}$ began to dominate the spectra. This is most likely the root cause of the suppression of individual nanosheet signals. Few-layer nanosheets appear to have nearly no Si-O-Si signal, and the 470 and $>800 \text{ cm}^{-1}$ modes occur near dominant silicon ones. For the 470 cm^{-1} mode, intensity changes are attributed to tetrahedra rotation as the materials are cleaved, with the structure trending toward a *T-O-T-M* fundamental smectite-like composition (i.e., a silicate monolayer).^[24b,c] Additionally, increases in intensity for modes at shifts $>800 \text{ cm}^{-1}$ are associated with the polymerization of the nanosheets and non-bridging oxygen (i.e., edges).^[24b,c] Looking at the normalized intensity (*I*) ratio between the Si-O-Si and 470 cm^{-1} modes ($I_{\text{Si-O-Si}} / I_{470}$) as a function of $\langle t \rangle$ in Figure 4d, across all phyllosilicates, a $\langle t \rangle^2$ scaling was observed. Similarly, in Figure 4e, the ratio between the intensities of the Si-O-Si mode and a mode at $\approx 930 \text{ cm}^{-1}$ ($I_{\text{Si-O-Si}} / I_{930}$) was found to be directly proportional to $\langle A \rangle$. Essentially, the scaling reported here demonstrates that Raman spectroscopy can be applied to measure both the thickness (or layer number) and areal size of phyllosilicate nanosheets in a network.

2.4. Understanding Bandgap Variations

The use of UV-vis analysis, or specifically absorption spectra, is useful for its demonstrated ability to yield in situ information about material concentration and dimension.^[26] When making such measurements, what is believed to be absorption spectra are generally extinction spectra. Whereby the extinction spectra (*Ext*) are the resultant of the combined effects associated with absorption (*Abs*) and scattering components (*Sca*).^[20–26] Extinction in this case when using a spectrometer in transmission mode can be defined as $T = 10^{-Ext}$, where *T* is transmission. This can be rewritten as $\ln T = -Ext = -(Abs + Sca)$. Using the Beer-Lambert law, the coefficients of each component can be related to one another as $\epsilon_{\text{coeff}} = \alpha_{\text{coeff}} + \sigma_{\text{coeff}}$, where ϵ_{coeff} , α_{coeff} , and σ_{coeff} are the extinction, absorption, and scattering coefficients, respectively. With our nanosheets suspended in liquid, it facilitated the use of UV-vis spectroscopy to measure the extinction spectra of our phyllosilicates like fuchsite in Figure 5a as a function of RCF. We observed the spectra of all materials to be highly dependent on the level of exfoliation and allowed information on concentration, dimension, and structure to be obtained (Figures S31–S39, Supporting Information).

For materials that have lateral lengths of $L < 50 \text{ nm}$, like in the case of our phyllosilicate nanosheets here, scattering was reported to be minimized,^[27] resulting in $\epsilon_{\text{coeff}} \approx \alpha_{\text{coeff}}$. Thus, for our suspensions, due to the small lateral size of our nanosheets, we could relate our extinction spectra directly to the absorption properties of the materials. This allowed for the direct calculation of the optical bandgap via Tauc plots from the UV-vis spectra (Figure S40, Supporting Information) without the need for

an integrating sphere to isolate the scattering component. Information with regards to nanosheet E_g was then combined with AFM statistics for different RCF samples to examine the effects of nanosheet dimensions. For fuchsite in Figure 5b, E_g increased from ≈ 3.1 to $\approx 3.75 \text{ eV}$ as the dimensions of the nanosheets decreased. With both values being far below the bulk's. Specifically, as a function of thickness in Figure 5c, for all phyllosilicates, E_g increased from ≈ 3 to $\approx 4.5 \text{ eV}$ as *t* decreased according to a power-law like scaling with an exponent of -0.16 . A similar scaling was also seen in TMDs (Figure S41, Supporting Information). The scaling here, however, incorrectly implies that phyllosilicates in bulk would trend toward being a low E_g semiconductor. This apparent finding is in direct opposition to past reports using DFT^[11f,12b] and ME.^[11e,f] In these studies, E_g decreased with layer number due to lattice relaxation. We believe it has been wrongly assumed that lattice relaxation is the only contributor to E_g variations in phyllosilicates. Particularly, as there is no correlation between the values reported by the two modes of study.

Plotting literary values from DFT and ME studies alongside our data in Figure 5c, we first note that DFT predicts much larger values for E_g than experimentally measured ones via ME. Second, both datasets follow different power-laws, like scaling. For DFT, values increased from ≈ 4 to $\approx 4.7 \text{ eV}$ as *t* increased from 1 to 3 nm. With the data roughly sitting on a fit with an exponent of 0.16. We note that this power-law scaling mirrors our LPE data, where we report an exponent of -0.16 . For ME, E_g increased from ≈ 1.6 to $\approx 6.7 \text{ eV}$ as *t* increased from 1 to 10 nm, following a $t^{0.5}$ scaling. We believe that the discrepancy between the two modes of investigation is due to a lack of consideration for quantum confinement effects (QCE). Like nanoribbons of graphene,^[28] as the nanosheets narrow, an E_g is introduced. For the DFT studies, nanosheets have a small ($\approx \text{nm}$) areal size due to the limitations associated with calculations. This means that QCE would be a constant effect that raises E_g , with variations in its value due to lattice relaxation. For the ME studies, the nanosheets had a large ($\approx \mu\text{m}$) areal size. Thus, no QCE occurs, and E_g is controlled only by relaxation. This then gives rise to reported values being much lower. We see that our data in Figure 5c bridges the gap between the two modes of study due to the fine control LPE allows for nanosheet dimension. Our $t^{-0.16}$ scaling is reflective of QCE being minimized as *A* increased with *t*. This QCE data bridging was exemplified by the observation that E_g values for LPE, ME, and DFT with comparable nanosheet thicknesses presented similar values. Specifically for $t \approx 2 \text{ nm}$, both LPE and DFT report E_g to be $\approx 4 \text{ eV}$. When $t \approx 4 \text{ nm}$, LPE and ME agree that $E_g \approx 3.4 \text{ eV}$. These findings further validate the utility associated with the dimensional control offered by liquid processing methods. Additionally, LPE approaches for phyllosilicates present a path toward the large-scale production of a single nanosheet type with finely tuned electronic properties that could vary between semi-metallic and insulating behaviors.

For QCE, the effect of nanomaterial dimensions on E_g can be generally written as $E_g \propto L^{-2}$.^[29] However, for our nanosheets we found through AFM that $L \propto W$. Thus, our nanosheets, are roughly square-shaped, and we can assume that $L^2 \propto A$. Leading to the QCE relationship,

$$E_g \propto A^{-1} \quad (2)$$

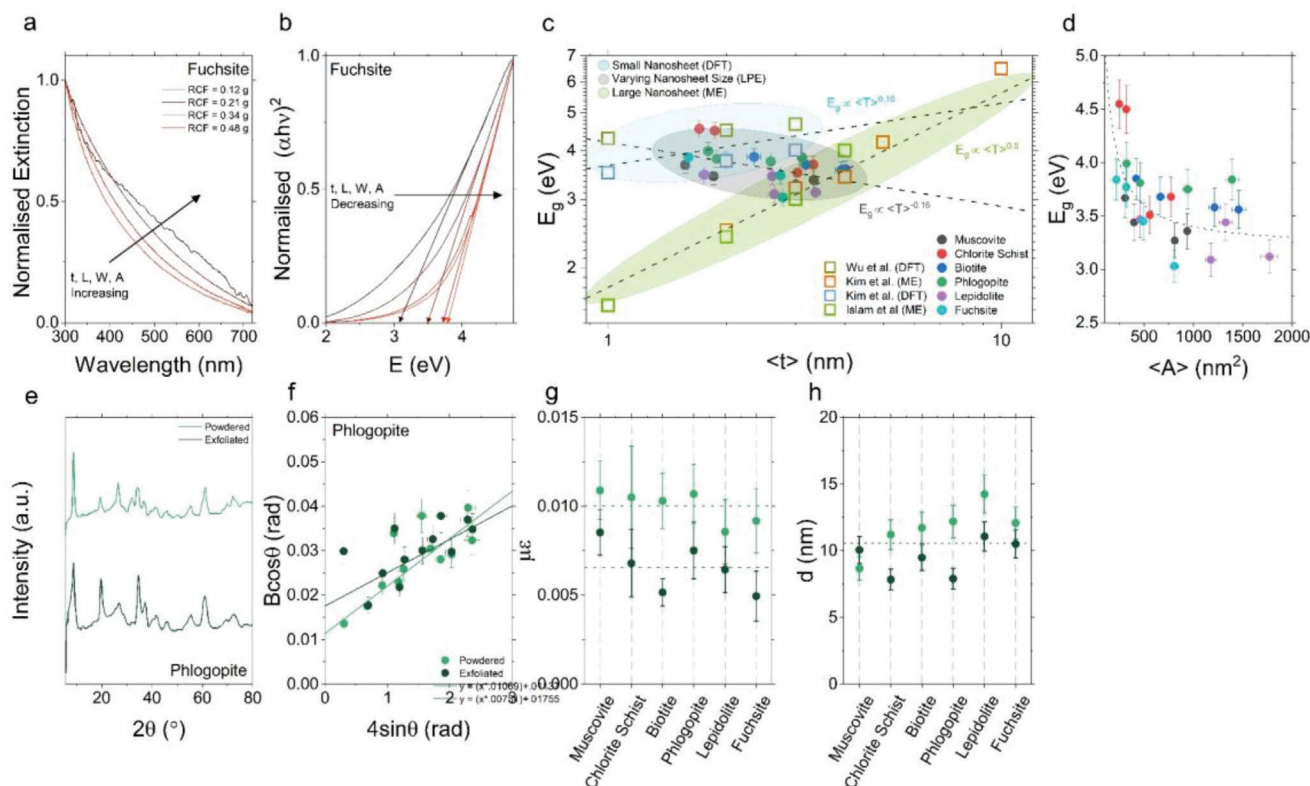


Figure 5. Optical and diffraction characterization of phyllosilicate nanosheets. a) Extinction spectra of fuchsite nanosheet suspensions as a function of RCF rate. b) Tauc plot derived from UV–vis analysis of size selected fuchsite nanosheet suspensions showed bandgap increasing with decreasing nanosheet dimensions. c) Bandgap (E_g) for LPE phyllosilicate materials versus mean nanosheet thickness ($\langle t \rangle$) in the gray bubble increased with diminishing values of $\langle t \rangle$ with a power-law exponent of -0.16 (gray-dashed line). In the blue and green bubbles, respectively, literary DFT^[11f,12b] and ME^[11e,f] data also presented power-law scaling with exponents of 0.16 (blue-dashed line) and 0.5 (green-dashed line), respectively. d) Due to the exfoliation mechanism dictated by Figure 3e–g, $\langle L \rangle \propto \langle W \rangle$ resulted in the mean nanosheet area ($\langle A \rangle$, i.e., $\langle L \rangle \times \langle W \rangle$) expectedly scaling as $\langle A \rangle^{-1}$ per Equation 2. e) Powder XRD spectra of powdered and exfoliated phlogopite. f) Williamson–Hall plot derived from the XRD data of phlogopite in (e). Solid lines represent linear fits of Equation 3 to derive lattice microstrain (μ , fit slope) and crystallite size (d , fit intercept), with values for each phyllosilicate type (powdered and exfoliated) plotted in (g) and (h), respectively.

We confirm this by plotting E_g as a function of A in Figure 5d, where we find good agreement with Equation 2's fit. We thus have confirmation that QCE contributes greatly to the change in E_g for small phyllosilicate nanosheets. Furthermore, the more standard description of QCE still applied, with E_g proportional to both L^{-2} and W^{-2} in Figure S42 (Supporting Information).

To quantitatively describe the lattice relaxation that caused the initial drop in E_g between bulk and exfoliated phyllosilicates, we modeled X-ray powder diffraction (XRD) spectra (Figure 5e; Figure S43, Supporting Information) using Williamson–Hall (W–H) analysis.^[30] The total broadening (B) of XRD peaks can be associated with two factors: microstrain (μ) and crystallite size (d).^[31] These contributions can be described using the linear W–H expression.

$$B \cos \theta = \mu \epsilon (4 \sin \theta) + \frac{K \lambda}{d} \quad (3)$$

where θ is the Bragg angle, K is the shape constant, which has a value of ≈ 0.9 , and λ is the X-ray wavelength. Plotting $B \cos \theta$ as a function of $4 \sin \theta$ in Figure 5f for bulk and exfoliated phlogopite, values for μ and d for this and all phyllosilicate materials

(Figure S43, Supporting Information) could be extrapolated from their respective Equation 3 fits. Plotting values for μ as a function of bulk and exfoliated material type in Figure 5g, on average we see values decreasing from ≈ 0.010 to ≈ 0.006 when going from the bulk to exfoliated state. We can confirm that lattice strain is the only factor contributing to peak broadening, as in Figure 5h we see that d has a constant value of ≈ 10.58 nm across all materials and stages of exfoliation. Furthermore, the values for μ and d reported here are consistent with previous studies on bulk phyllosilicates.^[32] We thus experimentally confirm that across all phyllosilicates, lattice relaxation occurs during delamination. Additionally, this relaxation resulted in band narrowing. However, the band narrowing was strongly controlled by QCE when the nanosheets were small.

2.5. Electrochemical Properties of Phyllosilicate Nanosheets

Past research has shown that smaller nanosheets are ideal for catalytic applications due to the abundance of edge sites that propagate reactions.^[33] We believe that with the small areal size associated with our phyllosilicate nanosheets and a recent obser-

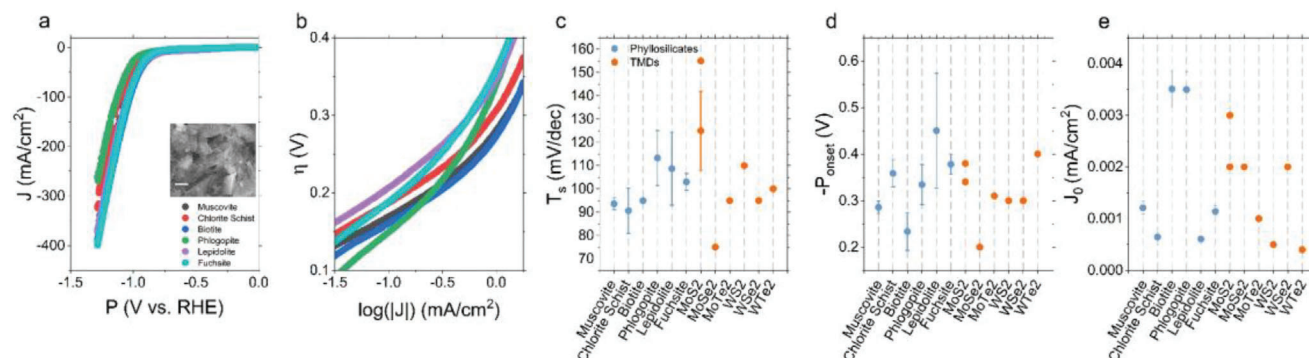


Figure 6. Catalytic properties of phyllosilicate nanosheet electrodes. a) Polarization curves for each phyllosilicate nanosheet type. Inset: SEM image of a lepidolite nanosheet electrode. b) Corresponding Tafel plots. c–e) Tafel slope (T_s), onset potential (P_{onset}), and exchange current density (J_0) as a function of micene and chlorene type, respectively, plotted alongside comparative liquid exfoliated transition metal dichalcogenides nanosheet electrodes.

vation that work function will decrease with layer number,^[34] micene and chlorene would be ideal candidates for highly effective HER electrochemical electrodes. By transferring filtered networks of phyllosilicate nanosheets onto glassy carbon, we created electrodes with constant density and thickness across all materials. This consistency is important for comparative analysis, as an electrode's electrochemical performance scales with both parameters.^[35] In **Figure 6a**, typical polarization curves for phyllosilicate nanosheet electrodes are shown, from which Tafel plots are formed in **Figure 6b**. Using the Butler–Volmer equation, current density (J) was related to exchange current density (J_0) overpotential (η), and Tafel slope (T_s) through $J = -J_0 \times 10^{\frac{\eta}{T_s}}$. Critical performance metrics T_s , onset potential (P_{onset}) and J_0 , for all phyllosilicates were then extrapolated and plotted alongside TMD literary data (**Figure 6c–e**). TMDs being arguably one of the most effective families of 2D materials for HER, and for good comparative analysis, we compare our work with TMD electrodes of similar density and thickness.^[35,36] For a material to be an effective catalysis for HER, ideally T_s , and P_{onset} are minimized, while J_0 is maximized. In comparison to TMDs, we found the catalytic performances of phyllosilicates like biotite, with its combination of performance metrics $T_s \approx 95 \text{ mV dec}^{-1}$, $P_{\text{onset}} \approx -0.234 \text{ V}$ and $J_0 \approx 0.0035 \text{ mA cm}^{-2}$, to far exceed those of other materials. In comparison, the most effective TMD, MoSe_2 ,^[36] presented values of $T_s \approx 75 \text{ mV dec}^{-1}$, $P_{\text{onset}} \approx -0.2 \text{ V}$, and $J_0 \approx 0.002 \text{ mA cm}^{-2}$. One critical difference is the natural abundance of biotite and other phyllosilicates, which lends well to both their low cost of production and effectiveness as alternatives to artificially procured materials like many TMDs. Definitively, we disprove the narrative that phyllosilicates are inert materials.

3. Conclusion

The LPE of phyllosilicate minerals presented nanosheets with highly tuneable electronic properties and superlative catalytic performances. These findings are in stark contrast to the common belief that the materials are insulating and inert. Through rigorous characterization, we detail the mechanisms that control nanosheet properties and believe that the work unlocks the potential this broadly untapped family of 2D materials can have for future optoelectronic, energy, and logic devices.

4. Experimental Section

Materials: Bulk phyllosilicates of chlorite schist (Scotland), biotite (Norway), phlogopite (Norway), lepidolite (Brazil), and fuchsite (Norway) mica materials were purchased from a commercial supplier (Geology Superstore). The muscovite (Ireland) sample was procured by Matilda McCabe at Glendalough, Co. Wicklow.

Processed Phyllosilicate Powders: Each phyllosilicate had a mass of $\approx 2 \text{ g}$ removed from the bulk crystal, which was then powdered using a commercial coffee grinder (UUOUU 200 W Bowl Spice Grinder). The powder was then shear mixed in deionized water (20 mg mL^{-1}) at 5000 rpm for 1 h at room temperature, after which the mixture was centrifuged at 5000 rpm. The supernatant was discarded, and the sediment was redispersed in IPA (20 mg mL^{-1}) using an ultrasonic tip (Sonics Vibra-cell VCX130, flathead probe) for 1 h at 60% amplitude and a configuration of 6 s on, 2 s off while being chilled ($\approx 5^\circ \text{C}$). The mixture was centrifuged at 5000 rpm, with the supernatant again discarded and the sediment kept. Sediment was dried at 60°C overnight and used as the starting material.

Liquid Phase Exfoliation of Phyllosilicates: The clean, powdered phyllosilicates were mixed into a sodium cholate solution (Sigma–Aldrich BioXtra, $\geq 99\%$, 6 mg mL^{-1}) at 2 mg mL^{-1} and ultrasonicated (Sonics Vibra-cell VCX130, flathead probe) for 5 h at 60% amplitude in a configuration of 6 s on, 2 s off while being chilled ($\approx 5^\circ \text{C}$). The resultant suspension was cascade centrifuged at 0.12, 0.21, 0.34, and 0.48 g using a previously developed method.^[20]

X-Ray Photoelectron Spectroscopy: Measurements were done in a Kratos Axis SUPRA spectrometer employing a monochromatic Al $K\alpha$ (1486.6 eV) X-ray source. Survey spectra were obtained with an energy step of 1 and 160 eV analyzer pass energy. The spectra were analyzed using CASA XPS software. Shirley baselines were used to subtract the background for quantification purposes. The spectra were calibrated using the B.E. of the C 1s peak at 284.5 eV due to the use of the charge neutralizer during the spectra acquisition.

Transmission Electron Microscopy: Phyllosilicate powder samples (RCF = 0.21 g) were dispersed in ethanol, drop-cast on 300-mesh carbon-coated copper grids, and dried. TEM measurements were performed in an image-corrected FEI (Thermo Fisher) Titan Cube with a spherical aberration corrector at the objective lens and operating at 300 kV. The electron dose was optimized to reduce any beam-induced damage to the samples during the measurements.

Atomic Force Microscopy: Size-selected suspensions of each phyllosilicate were drop-cast onto a heated silicon wafer ($\approx 70^\circ \text{C}$). After deposition, wafers were washed with deionized water to remove residual surfactant. For measurements, an atomic force microscope (AFM) Dimension® icon Bruker positioned in an insulated box over an anti-vibrant stage to minimize environmental noise and building vibrations was employed. The probe used was a ScanAsyst Air tip with a spring constant of 0.4 N m^{-1} ,

and a tip-sample contact force of 5.0 nN was used for all measurements. For all samples, the scan size of 2 μm was used to collect thickness, width, and length data for individual nanosheets. To obtain a good statistical average, 200 measurements for each sample were performed through line profiles and ImageJ.

UV-Vis Spectroscopy: Measurements of dispersions were performed using a Shimadzu UV-3600 Plus spectrophotometer from 200 to 800 nm using a quartz cuvette (path length, 1 cm). The sample curves were an average of five spectra.

Raman Spectroscopy: Suspensions of size selected nanosheets for each phyllosilicate were drop-cast onto a glass slide. For the processed starting powder, the material was heaped on a glass slide and patted flat with a spatula. For the bulk materials, a large flake was removed from the bulk crystal and laid flat on a glass slide. Measurements were carried out using a Renishaw inVia confocal Raman microscope with 0.8 cm^{-1} spectral resolution and a 532 nm laser (type: solid state, model: RL53250). The 2400 mm^{-1} grating at 100 \times magnification and 5 mW laser power are used. For each sample curve, an average of ten spectra was used.

Mechanical Exfoliation and Characterization: A small flake was taken off each phyllosilicate bulk crystal using tweezers, and each was placed onto the adhesion side of Nitto Deko SPV 224 tape. Using a previously developed method,^[37] the flakes were repeatedly peeled, with subsequent delaminated flakes formed and transferred onto a silicon wafer. Using an optical microscope (Olympus BX53M with a 4K digital CCD camera), flake location was noted, and AFM was applied to measure morphological properties (thickness and lateral size). Raman was performed on each flake, with spectra taken as a function of distance from the flake's center. The laser beam was moved in increments of 0.5 μm from the center to the flake's edge, with ten total measurement steps taken.

X-Ray Powder Diffraction: Suspensions of nanosheets (RCF = 0.21 g) were filtered onto nitrocellulose membranes (25 nm pore size) and washed with 1 L of deionized water to remove residual surfactant and create a thin film of material. After which, the membrane was left in the oven at 60 $^{\circ}\text{C}$ overnight to dry. Material was then scraped for the membranes using a spatula, and the resultant nanosheet powder was collected in a plastic capillary tube. The data were collected on a Rigaku Gemini Ultra using the powder mode in the CrysAlisPro (version 171.42.75) software. The data was collected using Cu radiation (1.5418 Å) over a range of 125 $^{\circ}$ in 2θ .

Electrochemical Electrode Formation and Analysis: Suspensions of phyllosilicate nanosheets (RCF = 0.34 g) of known concentration found via vacuum filtration were filtered onto nitrocellulose membranes (25 nm pore size) and washed with 1 L of deionized water to remove residual surfactant. Nanosheet networks of density $0.1 \text{ mg cm}^{-2} \pm 0.03$, measured through network mass/area ratio, and thickness of $300 \text{ nm} \pm 100 \text{ nm}$, measured via profilometry (Bruker DektakXT), were obtained. The membranes with the deposition of the nanosheets were then cut into pieces and transferred onto glassy carbon rods (3 mm diameter, BASi). Transfer was done by placing the membrane (network side down) on the substrate, wetting the film with isopropanol, and applying pressure. Acetone vapor and baths were used to dissolve the membrane, leaving the network on the substrate. Electrochemical tests consisted of linear sweep voltammetry and electrochemical impedance spectroscopy using a Gamry Reference 3000 potentiostat in a three-electrode configuration. The glassy carbon electrode was used as the working electrode, while a platinum wire and Ag/AgCl (3 M KCl) were used as the counter and the reference electrode, respectively. Linear sweep voltammetry experiments were performed with a scan rate of 5 mV s^{-1} from 0 to -1.5 V (vs RHE) in 0.5 M H_2SO_4 to investigate the hydrogen evolution performance. The measured potential was converted to the RHE scale by adding +0.2 V, measured with respect to a Gaskatel Hydroflex H_2 reference electrode.

Scanning Electron Microscopy: Representative topological images of electrochemical electrodes were attained by drop-casting a suspension (RCF = 0.34 g) onto a silicon wafer. The wafer was then attached to a scanning electron microscope (SEM) stub using a carbon tab and silver paint. The topography of the nanosheet network was examined using a Zeiss SIGMA field emission gun SEM (FEG-SEM) in SE2 mode at 10 kV.

Supporting Information

Supporting Information is available from the Wiley Online Library or from the author.

Acknowledgements

The authors acknowledge funding through the University of Sussex Strategic Develop Fund and the Saudi Arabian Cultural Bureau. R.A. acknowledges funding from the Spanish MCIN (project grant PID2019-104739GB-I00/AEI/10.13039/501100011033), the Government of Aragon (project DGA E13-20R), and the European Union H2020 program "ESTEEM3" (823717).

Conflict of Interest

The authors declare no conflict of interest.

Author Contributions

C.S.B. conceived and designed experiments. C.W. created all samples for the study. C.W., A.J., M.T., A.K.A.A., J.P.S., and S.M.R. performed experiments. C.S.B. analyzed and modeled data. J.P.S., S.M.R., R.A., and C.S.B. contributed materials, tools, and supervision. C.S.B. wrote the paper with input from R.A. and A.R.

Data Availability Statement

The data that support the findings of this study are available in the supplementary material of this article.

Keywords

chlorite, liquid exfoliation, mica, nanosheets, tuneable bandgap

Received: April 17, 2023

Revised: May 31, 2023

Published online:

- [1] C. Backes, A. M. Abdelkader, C. Alonso, A. Andrieux-Ledier, R. Arenal, J. Azpeitia, N. Balakrishnan, L. Banszerus, J. Barjon, R. Bartali, et al., *2D Mater.* **2020**, *7*, 022001.
- [2] A. J. Ryan, C. J. Kearney, N. Shen, U. Khan, A. G. Kelly, C. Probst, E. Brauchle, S. Bicca, C. D. Garciaarena, V. Vega-Mayoral, P. Loskill, S. W. Kerrigan, D. J. Kelly, K. Schenke-Layland, J. N. Coleman, F. J. O'Brien, *Adv. Mater.* **2018**, *30*, 1706442.
- [3] C. J. Zhang, S. H. Park, A. Seral-Ascaso, S. Barwich, N. McEvoy, C. S. Boland, J. N. Coleman, Y. Gogotsi, V. Nicolosi, *Nat. Commun.* **2019**, *10*, 849.
- [4] Y. Hernandez, V. Nicolosi, M. Lotya, F. M. Blighe, Z. Sun, S. De, I. T. McGovern, B. Holland, M. Byrne, Y. K. Gun'Ko, J. J. Boland, P. Niraj, G. Duesberg, S. Krishnamurthy, R. Goodhue, J. Hutchison, V. Scardaci, A. C. Ferrari, J. N. Coleman, *Nat. Nanotechnol.* **2008**, *3*, 563.
- [5] J. N. Coleman, M. Lotya, A. O'Neill, S. D. Bergin, P. J. King, U. Khan, K. Young, A. Gaucher, S. De, R. J. Smith, I. V. Shvets, S. K. Arora, G. Stanton, H.-Y. Kim, K. Lee, G. T. Kim, G. S. Duesberg, T. Hallam, J. J. Boland, J. J. Wang, J. F. Donegan, J. C. Grunlan, G. Moriarty, A. Shmeliov, R. J. Nicholls, J. M. Perkins, E. M. Grieveson, K. Theuvsen, D. W. McComb, P. D. Nellist, et al., *Science* **2011**, *331*, 568.

- [6] D. McAteer, I. J. Godwin, Z. Ling, A. Harvey, L. He, C. S. Boland, V. Vega-Mayoral, B. Szydłowska, A. A. Rovetta, C. Backes, J. B. Boland, X. Chen, M. E. G. Lyons, J. N. Coleman, *Adv. Energy Mater.* **2018**, *8*, 1702965.
- [7] M. Naguib, M. Kurtoglu, V. Presser, J. Lu, J. Niu, M. Heon, L. Hultman, Y. Gogotsi, M. W. Barsoum, *Adv. Mater.* **2011**, *23*, 4248.
- [8] a) A. G. Kelly, D. O'Suilleabhain, C. Gabbett, J. N. Coleman, *Nat. Rev. Mater.* **2022**, *7*, 217; b) Q. H. Wang, K. Kalantar-Zadeh, A. Kis, J. N. Coleman, M. S. Strano, *Nat. Nanotechnol.* **2012**, *7*, 699.
- [9] a) D. S. Baik, K. S. No, J. S.-S. Chun, Y. J. Yoon, *J. Am. Ceram. Soc.* **1995**, *78*, 1217; b) R. Frisenda, Y. Niu, P. Gant, M. Muñoz, A. Castellanos-Gomez, *npj 2D Mater. Appl.* **2020**, *4*, 38.
- [10] H. H. Poole, *J. Sci.* **1916**, *32*, 112.
- [11] a) L. Mogg, G. P. Hao, S. Zhang, C. Bacaksiz, Y. C. Zou, S. J. Haigh, F. M. Peeters, A. K. Geim, M. Lozada-Hidalgo, *Nat. Nanotechnol.* **2019**, *14*, 962; b) X. Zou, J. Xu, L. Liu, H. Wang, W.-M. Tang, *Nanotechnology* **2020**; c) C. Wei, W. Zhao, X. Shi, C. Pei, P. Wei, J. Zhang, H. Li, *Langmuir* **2019**, *35*, 5130; d) T. Arai, K. Sato, A. Iida, M. Tomitori, *Sci. Rep.* **2017**, *7*, 4054; e) M. R. Islam, M. Tomitori, *Appl. Surf. Sci.* **2020**, *532*, 147388; f) S. S. Kim, T. V. Khai, V. Kulish, Y.-H. Kim, H. G. Na, A. Katoch, M. Osada, P. Wu, H. W. Kim, *Chem. Mater.* **2015**, *27*, 4222.
- [12] a) J. Mukherjee, M. H. Dalsaniya, S. Bhowmick, D. Bhowmik, P. K. Jha, P. Karmakar, *Surf. Interfaces* **2022**, *33*, 102283; b) S. Wu, W. P. C. Lee, P. Wu, *Sci. Rep.* **2022**, *12*, 2868.
- [13] a) F. Jia, S. Song, *RSC Adv.* **2015**, *5*, 52882; b) F. Jia, J. Su, S. Song, *Colloids Surf. A* **2015**, *471*, 19; c) F. Jia, B. Yang, Q. Wan, S. Song, *Comp. Mater. Sci.* **2017**, *132*, 74; d) F. Jia, L. Yang, Q. Wang, S. Song, *RSC Adv.* **2017**, *7*, 1082; e) T. V. Khai, H. G. Na, D. S. Kwak, Y. J. Kwon, H. Ham, K. B. Shim, H. W. Kim, *Nanotechnology* **2013**, *24*, 145602; f) X.-F. Pan, H.-L. Gao, Y. Lu, C.-Y. Wu, Y.-D. Wu, X.-Y. Wang, Z.-Q. Pan, L. Dong, Y.-H. Song, H.-P. Cong, S.-H. Yu, *Nat. Commun.* **2018**, *9*, 2974; g) W. Ying, B. Han, H. Lin, D. Chen, X. Peng, *Nanotechnology* **2019**, *30*, 385705.
- [14] A. Castellanos-Gomez, M. Wojtaszek, N. Tombros, N. Agrait, B. J. van Wees, G. Rubio-Bollinger, *Small* **2011**, *7*, 2491.
- [15] F. Zeng, X. Chen, G. Xiao, H. Li, S. Xia, J. Wang, *ACS Nano* **2020**, *14*, 611.
- [16] H. N. Khoury, *Arab J. Geosci.* **2019**, *12*, 706.
- [17] G. A. Carson, S. Granick, *J. Mater. Res.* **1990**, *5*, 1745.
- [18] J. W. Obreimoff, P. L. Kapitza, *Proc. Math. Phys. Eng. Sci.* **1930**, *127*, 290.
- [19] C. Elmi, S. Guggenheim, R. Gieré, *Clays Clay Miner.* **2016**, *64*, 537.
- [20] C. Backes, B. M. Szydłowska, A. Harvey, S. Yuan, V. Vega-Mayoral, B. R. Davies, P.-I. Zhao, D. Hanlon, E. J. G. Santos, M. I. Katsnelson, W. J. Blau, C. Gadermaier, J. N. Coleman, *ACS Nano* **2016**, *10*, 1589.
- [21] C. Backes, D. Campi, B. M. Szydłowska, K. Synnatschke, E. Ojala, F. Rashvand, A. Harvey, A. Griffin, Z. Sofer, N. Marzari, J. N. Coleman, D. D. O'Regan, *ACS Nano* **2019**, *13*, 7050.
- [22] H. Kaur, J. N. Coleman, *Adv. Mater.* **2022**, *34*, 2202164.
- [23] T. Carey, O. Cassidy, K. Synnatschke, E. Caffrey, J. Garcia, S. Liu, H. Kaur, A. G. Kelly, J. Munuera, C. Gabbett, D. O'Suilleabhain, J. N. Coleman, *ACS Nano* **2023**, *17*, 2912.
- [24] a) C. Arbiol, G. D. Layne, *Appl. Spectrosc.* **2021**, *75*, 1475; b) A. Wang, J. J. Freeman, B. L. Jolliff, *J. Raman Spectrosc.* **2015**, *46*, 829; c) A. Tlili, D. C. Smith, J. M. Beny, H. Boyer, *Mineral. Mag.* **1989**, *53*, 165.
- [25] H. Malekpour, A. A. Balandin, *J. Raman Spectrosc.* **2018**, *49*, 106.
- [26] C. Backes, R. J. Smith, N. McEvoy, N. C. Berner, D. McCloskey, H. C. Nerl, A. O'Neill, P. J. King, T. Higgins, D. Hanlon, N. Scheuschner, J. Maultzsch, L. Houben, G. S. Duesberg, J. F. Donegan, V. Nicolosi, J. N. Coleman, *Nat. Commun.* **2014**, *5*, 4576.
- [27] A. Harvey, C. Backes, J. B. Boland, X. He, A. Griffin, B. Szydłowska, C. Gabbett, J. F. Donegan, J. N. Coleman, *Nat. Commun.* **2018**, *9*, 4553.
- [28] a) T. Wassmann, A. P. Seitsonen, A. M. Saitta, M. Lazzeri, F. Mauri, *Phys. Rev. Lett.* **2008**, *101*, 096402; b) X. Li, X. Wang, L. Zhang, S. Lee, H. Dai, *Science* **2008**, *319*, 1229.
- [29] a) L. E. Brus, *J. Chem. Phys.* **1984**, *80*, 4403; b) S. Parveen, P. K. Prasanna, S. Chakraborty, P. K. Giri, *J. Mater. Chem. C* **2021**, *9*, 2437; c) H. Yu, J. Li, R. A. Loomis, L.-W. Wang, W. E. Buhro, *Nat. Mater.* **2003**, *2*, 517.
- [30] S. Bagherian, A. K. Zak, *Mater. Sci. Semicond. Process.* **2016**, *56*, 52.
- [31] a) A. Khorsand Zak, W. H. A. Majid, M. E. Abrishami, R. Yousefi, *Solid State Sci.* **2011**, *13*, 251; b) V. D. Mote, Y. Purushotham, B. N. Dole, *J. Theor. Appl. Phys.* **2012**, *6*, 6.
- [32] a) R. J. Merriman, B. Roberts, D. R. Peacor, *Contr. Mineral. Petrol.* **1990**, *106*, 27; b) R. J. Merriman, B. Roberts, D. R. Peacor, S. R. Hiron, *J. Metamorph. Geol.* **1995**, *13*, 559; c) P. J. Sánchez-Soto, M. Macías, J. L. Pérez-Rodríguez, *J. Am. Ceram. Soc.* **1993**, *76*, 180.
- [33] J. Xie, H. Zhang, S. Li, R. Wang, X. Sun, M. Zhou, J. Zhou, X. W. Lou, Y. Xie, *Adv. Mater.* **2013**, *25*, 5807.
- [34] A. Arora, K. L. Ganapathi, T. Dixit, M. Miryala, M. Masato, M. S. R. Rao, A. Krishnan, *Phys. Rev. Appl.* **2022**, *17*, 064042.
- [35] D. McAteer, Z. Gholamvand, N. McEvoy, A. Harvey, E. O'Malley, G. S. Duesberg, J. N. Coleman, *ACS Nano* **2016**, *10*, 672.
- [36] Z. Gholamvand, D. McAteer, C. Backes, N. McEvoy, A. Harvey, N. C. Berner, D. Hanlon, C. Bradley, I. Godwin, A. Rovetta, M. E. G. Lyons, G. S. Duesberg, J. N. Coleman, *Nanoscale* **2016**, *8*, 5737.
- [37] A. Castellanos-Gomez, M. Buscema, R. Molenaar, V. Singh, L. Janssen, H. S. J. v. d. Zant, G. A. Steele, *2D Mater.* **2014**, *1*, 011002.